Specificity and competition of mRNAs dominate droplet pattern in protein phase separation

Fei Xu,[1] Dingyang Miao,[1] Wei Li,[1] Jun Jin,[1] Zhilong Liu,[1] Chuansheng Shen ●,[2] Jiqian Zhang,[3] Jianwei Shuai,[1,4] and Xiang Li[1,*]

[1]*Department of Physics, Xiamen University, Xiamen 361005, China*
[2]*School of Mathematics and Physics, Anqing Normal University, Anqing, Anhui 246011, China*
[3]*Department of Physics, Anhui Normal University, Wuhu, Anhui 241000, China*
[4]*Oujiang Laboratory (Zhejiang Lab for Regenerative Medicine, Vision and Brain Health) and Wenzhou Institute, University of Chinese Academy of Sciences, Wenzhou, Zhejiang 325001, China*

Phase separation is a ubiquitous and emerging mechanism underlying intracellular organization. Yet how distinct molecular compositions in phase-separated condensates are established and what prohibits these condensates from randomly fusing together remain largely unanswered. Here, through proposing a Cahn-Hilliard phase-field model paired with Ginzburg-Landau free-energy scheme, we explored how compositions are assembled in messenger RNAs (mRNAs)-driven protein droplets with respect to distinct physical properties. By analyzing the intradroplet heteropatterning of two specific droplets (*CLN*3 mRNA- and *BNI*1 mRNA-driven Whi3 droplets), we demonstrated that the growth rate of droplet size and higher-order complexes assembly in droplet are severally determined by the diffusion rate of droplet and the binding rate of mRNA with protein. While considering the three-species mixed system of two mRNAs that share a common binding protein, the two specific droplets preferentially assemble separately rather than colocalize. We found the two droplets compete with each other by snatching the protein that has been recruited into the other droplet when the free protein is insufficient. Further analysis dissects that the gradient–interfacial energy coefficients, initial mRNAs levels, and mRNAs-protein binding rates can efficiently shift the spatial patterns of the two specific droplets from segregation to the shared interface or enclosed patterns. All three patterns obtained by tuning the initial mRNAs levels or mRNA-protein binding rates have been experimentally observed. Another unreported core-shell pattern is predicted by synergistically reducing the gradient and interfacial energy coefficients. Our findings shed light on the establishment of intradroplet compositions in condensates with distinct physical properties and the general control mechanisms of phase-separated pattern formation.

I. INTRODUCTION

Liquid-liquid phase separation (LLPS) appears to be emerging as a new principle for explaining the organization of living cells [1,2]. Evidence is now mounting that LLPS is a general and crucial mechanism for regulating biological functions by controlling the spatiotemporal distribution of intracellular biomacromolecules [3]. LLPS-driven partition of molecules into dense phases enables the disordered liquid molecules to form ordered functional compartments. Although these functional compartments are not enveloped by biofilms, they are structurally stable and are referred to as membraneless organelles [4]. Membraneless organelles, such as processing bodies, stress granules, and paraspeckles [5,6], are identified to be required in sensing stress signals,

maintaining intracellular homeostasis, and exerting functional responses [7–9]. Aberrant forms of LLPS frequently occur in various diseases, such as neurodegenerative diseases, immune diseases, amyotrophic lateral sclerosis, and cancer [10]. Recent studies have also revealed that the nucleocapsid protein triggers the main immune response in COVID-19 patients by interacting with viral messenger RNAs (mRNAs) to form LLPS droplets [11]. Understanding the molecular mechanisms of condensate assembly in LLPS is therefore of great significance for disease prevention and treatment [2,3,10].

Intrinsically disordered proteins (regions) are identified to encode a driving force for LLPS [12,13]. Whi3, a largely disordered protein with long PolyQ tracts adjacent to an RNA recognition motif (RRM) has been extensively studied [1,14–16]. The multivalent binding sites on Whi3 promote LLPS in cells through interacting with mRNAs, such as *CLN*3 (cyclin-encoding mRNA) and *BNI*1 (formin-encoding mRNA), altering the physical properties of Whi3 droplets such as viscosity, propensity to fuse, and so on. The optimal mRNA to Whi3 molar ratio for *BNI*1 is larger than that for *CLN*3, and BNI1-Whi3 droplet fuses faster than CLN3-Whi3 droplet. Besides, *CLN*3 binds with Whi3 to form LLPS droplet located around nuclei, while BNI1-driven

Whi3 droplet assembles at cell tips. CLN3-Whi3 droplet regulates cell cycle, but the BNI1-Whi3 droplet establishes polarity sites and modulates actin [1,14]. These distinct physical properties and functions imply the existence of intrinsic or compositional differences between these two types of droplets. Although these experimental phenomena were observed, how the distinct molecular compositions are established and maintained in droplets, and the spatiotemporal control of their assembly are poorly understood. More importantly, understanding the competition mechanism of these two mRNAs for protein to execute distinct cell functions is urgently needed.

Although the occurrence of LLPS droplets within cells is firmly established, a quantitative understanding of the droplet formation processes and mechanisms is still lacking. Thermodynamics provided a theoretical perspective for understanding phase separation in biomacromolecular interaction systems in previous studies [17,18]. However, compared to inanimate systems, living systems maintain a low-entropy state by actively consuming energy and are dissipative structural systems far from equilibrium. Developing coarsening models of linear irreversible thermodynamics to quantitatively describe the phase-separation process in living systems is a fundamental challenge [19]. A number of mathematical modeling studies have been well performed to explore the molecular interactions that enhance the formation of LLPS droplets. Both sharp and diffuse interfaces were considered to study droplets formation and spatial patterning [17,20–22]. Casior *et al.* previously investigated bivalent mRNA-protein interactions that regulate phase-separated intradroplet patterning, and further explored how two mRNAs share a common binding protein to create a heterogeneous droplet field [20,21]. Although these phenomenological models gave insights into the mechanisms of LLPS droplets formation to some extent, a quantitative understanding of droplets composition and distinct droplets established by multiple mRNA-protein species is still lacking. In addition, a quantitative analysis of specific droplets physical properties and control mechanisms is significant to provide potential clues to prevent and treat related diseases.

Although both *BNI*1 mRNA and *CLN*3 mRNA have five Whi3 binding sites, BNI1-Whi3 droplet and CLN3-Whi3 droplet exhibit structural differences and are assembled at different locations [15]. Motivated by a desire to understand how these two types of droplets exhibit distinct physical properties and their competition strategy for patterns formation, we proposed a Cahn-Hillard phase-field model paired with a Ginzburg-Landau free-energy scheme to describe the high-valence mRNA-protein interactions to form distinct complexes capable of phase separation [19–21,23]. Through illustrating the spatiotemporal heterogeneity, we found the intradroplet heteropatterning of these two droplets. The size of *BNI*1 droplet grows faster, while higher-order complexes assemble quicker in *CLN*3 droplet. Further analysis confirms that growth rate and higher-order complexes assembly are, respectively, determined by the diffusion rate of droplet and the binding rate of mRNAs with protein. *BNI*1 and *CLN*3 compete for Whi3 to establish a heterogeneous droplet field. *BNI*1 droplet and *CLN*3 droplet preferentially assemble separately, rather than by colocalization. We observed that *BNI*1 droplet snatches the Whi3 that has been recruited into *CLN*3 droplet
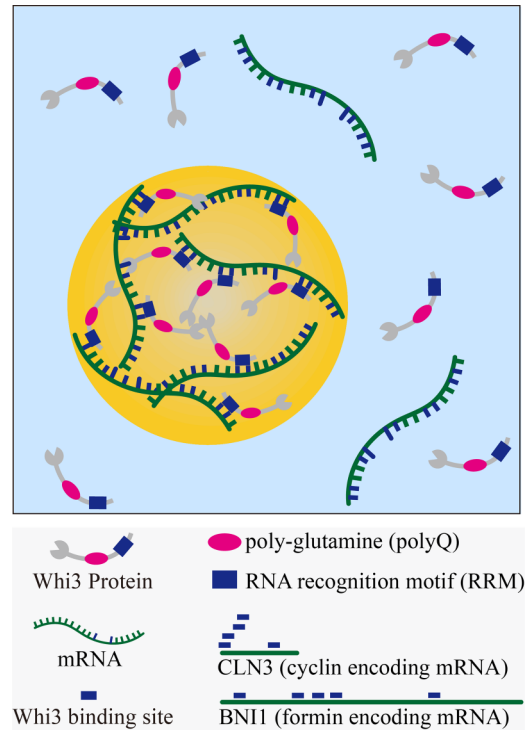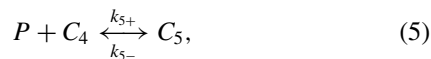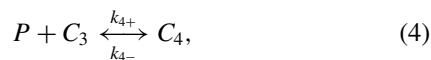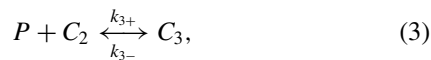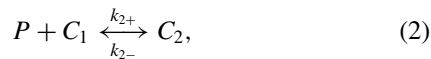

FIG. 1. Schematic illustration of the model for mRNA-driven Whi3 protein LLPS. Whi3 is a polyQ-containing RNA binding protein. Both *CLN*3 mRNA and *BNI*1 mRNA have five Whi3-binding sites, and *BNI*1 is four times longer than *CLN*3.

when the level of free Whi3 is insufficient. More importantly, the gradient–interfacial energy is found to determine whether these two types of droplets colocalize in a single condensate. Variation of the demixing energy coefficients efficiently shifts the spatial patterns of these two droplets from segregation to the shared interface pattern or enclosed pattern. Apart from the experimentally identified patterns, we predicted a droplet pattern of *CLN*3-core and *BNI*1-shell with the decrease of demixing energy coefficients. Finally, the function of initial mRNA levels and mRNA-protein binding rates are further discussed to address the diverse droplet patterns of spatiotemporal heterogeneity. Thus, through highlighting the distinct properties of different droplets and their competition, our study gives insights into the molecular mechanisms of condensate assembly in LLPS, providing guidance for future experiments and potential clues to develop more rational strategies for diseases.

II. MODELING THE SPATIAL PATTERN OF mRNA-PROTEIN DROPLET ASSEMBLY

Based on the Cahn-Hilliard diffuse interface model [19], we proposed a phase-field model to explore how protein phase separation are controlled by mRNAs. As illustrated in Fig. 1, free Whi3 protein and a type of mRNA are mixed, in which specific mRNA could bind to Whi3 through RRM to form complexes. The two types of mRNAs, *CLN*3 and *BNI*1, were reported to have five Whi3-binding sites, but the composition of mRNA-Whi3 complexes in the phase-separated droplets is unclear [1,14]. In our model, we thus considered up to five

proteins can bind to a single mRNA chain to form complexes which are capable of driving droplet assembly. The reversible chemical reactions for mRNA-protein binding and unbinding are as follows:

$$P + R \underset{k_{1-}}{\overset{k_{1+}}{\rightleftharpoons}} C_1, \tag{1}$$

$$P + C_1 \underset{k_{2-}}{\overset{k_{2+}}{\rightleftharpoons}} C_2, \tag{2}$$

$$P + C_2 \underset{k_{3-}}{\overset{k_{3+}}{\rightleftharpoons}} C_3, \tag{3}$$

$$P + C_3 \underset{k_{4-}}{\overset{k_{4+}}{\rightleftharpoons}} C_4, \tag{4}$$

$$P + C_4 \underset{k_{5-}}{\overset{k_{5+}}{\rightleftharpoons}} C_5, \tag{5}$$

where P refers to Whi3 protein and R refers to $CLN3$ mRNA or $BNI1$ mRNA. C_1 is the mRNA-protein complex of a single Whi3 protein that binds with a single mRNA through any one of the five binding sites. When another site of the rest four binding sites on the mRNA in C_1 complex binds to a second Whi3 protein, complex C_2 is formed. C_2 could further bind to Whi3 to form the complexes of C_3, C_4, and C_5 in turn. All these types of mRNA-protein complexes (C_1, C_2, C_3, C_4, and C_5) can trigger droplet assembly.

For simplicity, the system is assumed to be closed and the volume fraction of each component contains the required solvent [19,24]. The sum of the volume fraction of different complexes can be described by the order parameter (Ø) as a multicomponent mixture presented below:

$$\phi = C_1 + C_2 + C_3 + C_4 + C_5. \tag{6}$$

Free mRNA and protein mix freely within the matrix or droplets, and all molecules evolve with standard Fick diffusive dynamics [25]. The system evolves within a two-dimensional rectangular region $[0, L_x] \times [0, L_y]$, where $L_x = L_y$ in our simulation. The region is discretized into 100×100 grid points. At $t = 0$, there is no mRNA-protein complex in the system, that is, $C_i(x, y, 0) = 0$, $i \in [1,5]$. To reflect the spatial heterogeneity of the system, the initial volume fractions of protein and mRNA are taken to be uniform distribution at each grid point.

The governing equations for one type of mRNA to control the evolution of Whi3 LLPS are described as follows:

$$\frac{\partial P}{\partial t} = \nabla[\lambda_P M(\phi)\nabla P] + k_{1-}C_1 - k_{1+}PR + k_{2-}C_2 - k_{2+}PC_1$$
$$+ k_{3-}C_3 - k_{3+}PC_2 + k_{4-}C_4 - k_{4+}PC_3$$
$$+ k_{5-}C_5 - k_{5+}PC_4, \tag{7}$$

$$\frac{\partial R}{\partial t} = \nabla[\lambda_R M(\phi)\nabla R] + k_{1-}C_1 - k_{1+}PR, \tag{8}$$

$$\frac{\partial C_1}{\partial t} = \nabla \cdot \left[\lambda_{C_1} M(\phi)\nabla\left(\frac{\delta F}{\delta C_1}\right) \right] + k_{1+}PR - k_{1-}C_1$$
$$- k_{2+}PC_1 + k_{2-}C_2, \tag{9}$$

$$\frac{\partial C_2}{\partial t} = \nabla \left[\lambda_{C_2} M(\phi)\nabla\left(\frac{\delta F}{\delta C_2}\right) \right] + k_{2+}PC_1 - k_{2-}C_2$$
$$- k_{3+}PC_2 + k_{3-}C_3 \tag{10}$$

$$\frac{\partial C_3}{\partial t} = \nabla \cdot \left[\lambda_{C_3} M(\phi)\nabla\left(\frac{\delta F}{\delta C_3}\right) \right] + k_{3+}PC_2 - k_{3-}C_3$$
$$- k_{4+}PC_3 + k_{4-}C_4, \tag{11}$$

$$\frac{\partial C_4}{\partial t} = \nabla \left[\lambda_{C_4} M(\phi)\nabla\left(\frac{\delta F}{\delta C_4}\right) \right] + k_{4+}PC_3 - k_{4-}C_4$$
$$- k_{5+}PC_4 + k_{5-}C_5, \tag{12}$$

$$\frac{\partial C_5}{\partial t} = \nabla \left[\lambda_{C_5} M(\phi)\nabla\left(\frac{\delta F}{\delta C_5}\right) \right] + k_{5+}PC_4 - k_{5-}C_5, \tag{13}$$

where $M(\phi)$ is a nondimensional phase-dependent term that measures mobility and follows $M(\phi) \in (0, 1]$ [26]. The functional form of the mobility $M(\phi)$ depends on the specific characteristics of the phase-separation process and specific systems. A value of 0 indicates that the interface is completely blocked, while a value of 1 implies that the interface can move freely. For simplification, we have assumed that $M(\phi)$ is a constant value of 1, as suggested in previous studies [18,20]. The phase-dependent mobility is not incorporated in our model. Of course, introducing the mobility as a function of phase in future efforts will make our model better. F is the Ginzburg-Landau free-energy term with the unit of $k_B T$ (k_B is the Boltzmann constant and T is temperature) [19], and is defined below:

$$F = \int_{\Omega} \left(\frac{\varepsilon^2}{2}|\nabla\phi|^2 + \frac{\phi^2}{4\omega} \times [1 - \phi]^2 \right)dx. \tag{14}$$

Ginzburg-Landau free energy and Flory-Huggins free energy are two common approaches to describe the behavior of materials in certain conditions, specifically in the context of phase separation and the formation of complex structures [19]. Compared to Flory-Huggins free energy, Ginzburg-Landau free energy is a simpler form of free energy avoiding the logarithmic terms in the mixing entropy, which are not required to discuss the underlying basic principles [27]. Besides, the order parameter (volume fraction of condensates) exhibits spatial variation and fluctuations in our model, while Ginzburg-Landau free energy is better to capture the effects of spatial variations and fluctuations of the order parameter, which are important near the critical point of phase separation [28]. Thus, in our model, Ginzburg-Landau free energy was selected.

The region is discretized using the second-order finite-difference scheme and the time is discretized using the second-order semi-implicit backward difference formula [29–31]. The boundary conditions are set as follows:

$$\nabla\frac{\delta F}{\delta C_i} \cdot \mathbf{n} = 0, \nabla C_i \cdot \mathbf{n} = 0, \nabla P \cdot \mathbf{n} = 0, \nabla R \cdot \mathbf{n} = 0. \tag{15}$$

We first obtained random parameter regime of the phase-field model in a reasonable biological parameter space through Latin hypercube sampling [32–34], and then estimated the optimal parameter regime by fitting the experimental data.

TABLE I. Parameter definitions and default values for the model.

Parameter	Definition	mRNA-Protein		Units
		CLN3-Whi3	BNI1-Whi3	
λ_P	Effective diffusion rate of protein	9.17×10^{-4}	9.17×10^{-4}	$\mu m^2/s$
λ_R	Effective diffusion rate of mRNA	1.39×10^{-4}	1.39×10^{-4}	$\mu m^2/s$
λ_{Ci}[a]	Effective diffusion rate of C_i complex	5.56×10^{-5}	3.33×10^{-4}	$\mu m^2/s$
k_{1+}	Binding rate of protein and RNA to form C_1	6.11×10^{-4}	3.61×10^{-4}	1/s
k_{2+}	Binding rate of protein and C_1 to form C_2	2.78×10^{-4}	1.67×10^{-4}	1/s
k_{3+}	Binding rate of protein and C_2 to form C_3	2.22×10^{-4}	8.89×10^{-5}	1/s
k_{4+}	Binding rate of protein and C_3 to form C_4	1.39×10^{-4}	5.56×10^{-5}	1/s
k_{5+}	Binding rate of protein and C_4 to form C_5	1.11×10^{-4}	4.44×10^{-5}	1/s
k_{i-}[a]	Unbinding rate of C_i	2.78×10^{-5}	6.94×10^{-6}	1/s
ε	Gradient energy coefficient	0.01	0.01	
ω	Interfacial energy coefficient	0.25	0.25	

[a]The i takes an integer in [1,5].

III. RESULTS

A. Distinct physical properties of phase-separated condensates driven by mRNAs

We first sought to separately capture the experimentally observed distinct physical properties of *CLN*3 droplet and *BNI*1 droplet using our phase-field model. *BNI*1 droplet was reported to fuse faster than *CLN*3 droplet [14]. There are nine kinetic parameters for each individual phase-field model of *CLN*3 and *BNI*1 droplets assembly, including the intermolecular binding–unbinding rates, diffusion rates, and demixing energy coefficients (Table I). Through adjusting the model kinetic parameters, the spatiotemporal assembly dynamics of *CLN*3 droplet and *BNI*1 droplet are shown in Fig. 2(a). Simulation results indicate that the droplets formed by BNI1-Whi3 complexes are significantly larger than those formed by CLN3-Whi3 complexes at the initial stage of LLPS (at ∼2.3 h). *BNI*1 droplets reach the steady state (the droplet size remains constant) at about 8 h, while *CLN*3 droplets take longer (∼10 h) to evolve to the steady state. Thus, *BNI*1 drives Whi3 phase separation faster than *CLN*3, which is supported by the experimental observations [14]. We quantified the degree of phase separation through measuring the size of the droplets. As the workflow shown in Fig. 2(b), we pixelated the transient phase plot and measured the maximum distance in every single droplet. Time series of the largest droplet size triggered by *CLN*3 and *BNI*1 are, respectively, presented in Fig. 2(c), suggesting that not only do the *BNI*1 droplets assemble faster, but also larger than the *CLN*3 droplets.

Having reproduced the growth properties of these two types of droplets, we next examined how the droplets size are impacted by the initial volume fraction of mRNAs and Whi3. The phase diagrams of droplet assembly under different mRNAs and Whi3 initial volume fractions at 4 h are shown in Fig. 2(d). The size of these two droplets gets larger with the initial volume fraction of Whi3 increase. However, when the initial volume fraction of Whi3 is low (such as 0.5), BNI1 can form droplets at a relatively low level (such as 0.8), while CLN3 cannot. This suggests that BNI1 is more efficient than CLN3 in driving Whi3 phase separation. Actually, BNI1 is nearly four times longer than CLN3, with up to

6590 nucleotides compared to the 1596 nucleotides of CLN3. Although both CLN3 and BNI1 have five binding sites for Whi3 protein, the distribution of these sites on BNI1 is relatively uniform throughout the entire RNA chain, whereas four of the five sites on CLN3 are concentrated in a small region of the chain. These differences in RNA structure likely lead to distinct binding–unbinding rates of CLN3 and BNI1 to Whi3. Our model's fit values suggest that BNI1 has a higher affinity for Whi3 than CLN3, resulting in more efficient driving of Whi3 phase separation even at low initial levels. Moreover, the experimentally observed fusion of these two droplets was also well reproduced by our model [Fig. 2(e)]. As the initial volume fraction of Whi3 increases, the apparent droplet volume initially increases and then decreases [Fig. 2(f)]. For a fixed initial volume fraction of CLN3 at 1.0, the largest droplet volume is observed at around 3.8 for Whi3, while for BNI1, the largest droplet volume is observed at approximately 2.4 for Whi3. *Vitro* experiments determined that the optimal molar ratio of *BNI*1 to Whi3 is approximately twofold larger than that of *CLN*3 to Whi3 [14]. In line with the experimental findings, the linear fit analysis indicates that the optimal volume fraction ratio of BNI1 to Whi3 in simulations is about twofold larger than the ratio of CLN3 to Whi3 [Fig. 2(g)].

To reduce the number of free parameters, we consulted or estimated the parameters from previous studies, and the unknown parameters are constrained within rational ranges and then determined by qualitatively fitting experimental observations. There are three types of parameters in our model: diffusion rates of molecules, binding–unbinding rates, and energy coefficients (Table I). The energy coefficients were adopted from a previously published model [20]. However, there is no direct evidence to support the ranges of diffusion rates and binding–unbinding rates of molecules in our model. We further conducted a thorough analysis by randomly selecting nearly 1000 sets of parameters across a wide range of values. One hundred sets of parameters that were able to drive BNI1 droplets faster than CLN3 droplets were screened out (Fig. S1(a) [35]). The *t*-distributed stochastic neighbor embedding dimensionality reduction visualization result of these 100 parameter sets was presented in Fig. S1(b) [35],
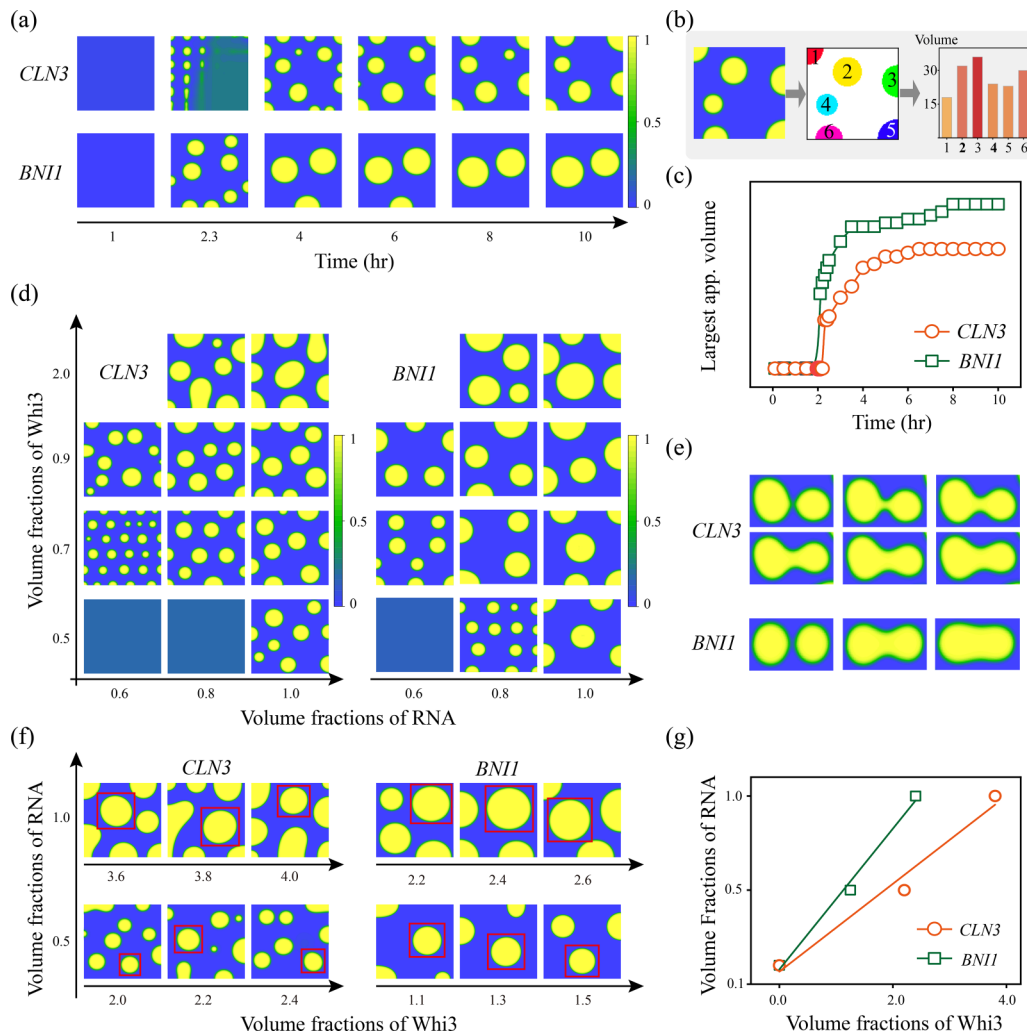
FIG. 2. $CLN3$ and $BNI1$ independently drive Whi3 LLPS with distinct physical properties. (a) Spatiotemporal dynamics of $CLN3$ droplets and $BNI1$ droplets. Initial volume fraction coefficients of mRNA and Whi3 were, respectively, set at 0.5 and 1.0. (b) Workflow of quantifying the size of droplets. (c) Time dependence of the largest droplet size driven by $CLN3$ and $BNI1$. (d) Phase diagrams of $CLN3$ droplets and $BNI1$ droplets at 4 h under different initial volume fractions of Whi3 and mRNAs. (e) $BNI1$ droplets fuse at a faster rate than $CLN3$ droplets. Time intervals between images are equal. (f) Initial volume fraction of mRNAs was fixed at 0.5 and 1.0, and the initial volume fraction of Whi3 corresponding to the complete largest apparent droplet volume at 4 h was determined. (g) Linear fitting of the optimal mRNAs/Whi3 initial volume fraction ratio for the largest droplet size.

suggesting that they all exhibited similar characteristics. Through selecting four representative parameter sets from different locations within the cluster, we found that only the parameter sets that close to our model could roughly reproduce the experimental observations of the optimal RNA/Whi3 molar ratio (Fig. S1(c) [35]). These results provide confidence that plausible parameter values were obtained in our model. Therefore, our model well reproduces the experimental observations of the distinct physical properties of $CLN3$ droplet and $BNI1$ droplet, providing a basis for further exploring the underlying regulatory mechanism of these two types of droplets.

B. Intradroplet discrepancy determined by complexes diffusion rate and mRNA-protein binding rate

To fully understand the distinct properties of $CLN3$ mRNA and $BNI1$ mRNA in driving Whi3 phase separation, the intradroplet constituents evolution of these two types of droplets are analyzed based on the original case shown in Fig 2(a). Spatiotemporal dynamics of the individual complexes within the droplets are shown in Figs. 3(a) and 3(b). The onset of $CLN3$- and $BNI1$-driven phase separation are, respectively, at $t = 2.43$ h and $t = 2.1$ h. Three typical time points after the onset are selected, and the corresponding phase diagrams indicate that the number of droplets driven by $CLN3$ is bigger than $BNI1$ while the droplet size of $BNI1$ is larger than $CLN3$ at each corresponding time point.

More intuitive constituent spatiotemporal evolution diagrams of $CLN3$ and $BNI1$ intradroplets are shown in Figs. 3(c) and 3(d). At the onset of phase separation, the droplets are heavily populated with C1 complex at the center, and only small amounts of C2 complex are uniformly distributed throughout the droplets. Higher-order complexes (C3, C4, and C5) form a ring structure at the droplets interface
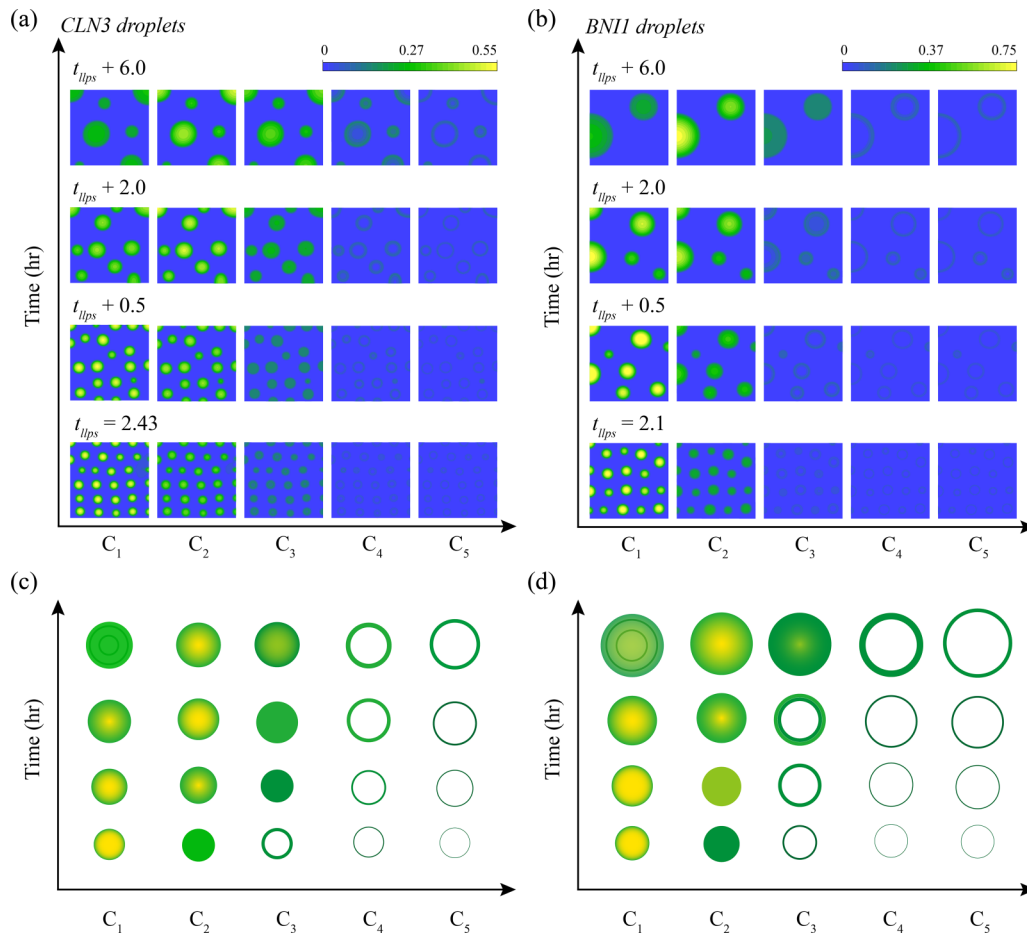
FIG. 3. Constituents spatiotemporal evolution of *CLN*3 and *BNI*1 intradroplets at four representative timepoints. (a) Patterns of *CLN*3-driven Whi3 LLPS at the onset of phase separation ($t = 2.43$ h), and at 0.5, 2.0, and 6.0 h after the onset of phase separation. (b) *BNI*1-driven Whi3 LLPS at the four typical time points. (c), (d) Schematic depicting the spatiotemporal evolution of constituents of *CLN*3 and *BNI*1 intradroplets.

with a quite low volume fraction. C1 complex continues to bind with Whi3 to form C2 complex, leading the volume fraction of C1 at the center to gradually decline but the size of droplets becomes larger with time increases. Simultaneously, C2 complex trends to become the dominant constituent at the center of the droplets. Higher-order complexes are distributed at the droplets interface and present a ring structure at the onset of phase separation. The ring droplets volume fraction increase and the droplets size get bigger over time, presenting a wavelike diffusion inward toward the droplet center. The patterns of higher-order complexes within *CLN*3 droplet and *BNI*1 droplet appear discrepant. The ring size of the higher-order complexes in *CLN*3 droplet is smaller than *BNI*1 droplet, but the ring width of *CLN*3 droplet is larger at the same time points after LLPS. Besides, at 0.5 h after LLPS, C3 complex fills the entire droplet uniformly of *CLN*3 intradroplet [Fig. 3(c)], while C3 complex still exhibits a ring structure at the interface of *BNI*1 droplet [Fig. 3(d)]. C3 complex fills the entire *BNI*1 droplet at 6.0 h after LLPS.

Next, differences of the higher-order complexes assembly between *CLN*3 and *BNI*1 intradroplets are further quantified [Figs. 4(a)–4(c)]. All the higher-order complexes in *CLN*3 droplets assemble faster than that in *BNI*1 droplets.

At the onset of LLPS, C_2 complex locates at the core of the *CLN*3 droplets and occupies 40% of the entire droplet size [Fig. 4(a)]. At 0.5 h after LLPS, C_2 complex dominates the entire *CLN*3 droplets, while C_2 complex in *BNI*1 droplets becomes the main part at 2 h after LLPS. The level threshold is fixed at 60% of all the complexes to quantify the size proportion of C_2 complex in the entire droplet. The size proportion of C_3 complex in *CLN*3 droplets is about threefold higher than that in *BNI*1 droplets at 6 h after LLPS [Fig. 4(b)]. Similar results are also obtained of C_4 and C_5 complexes and the proportion of C_4 complex in *CLN*3 droplets is extremely higher than that in *BINI* at 6 h after LLPS [Fig. 4(c)]. The distinct constituents spatiotemporal evolution between *CLN*3 and *BNI*1 intradroplets are primarily determined by the system parameters. As the adjusted parameters show in Table I, the binding rates (k_{i+}) of CLN3-Whi3 complexes are larger than BNI1-Whi3, which might result in the faster assembly of higher-order complexes in *CLN*3 droplets. However, the diffusion rates (λ_C) of BNI1-Whi3 complexes are bigger than CLN3-Whi3, possibly inducing the larger size formation of *BNI*1 droplets. To validate our conjecture, two-parameter analysis of the binding rates (k_{i+}) and the diffusion rates (λ_C) is performed and the results are shown in Figs. 4(d)
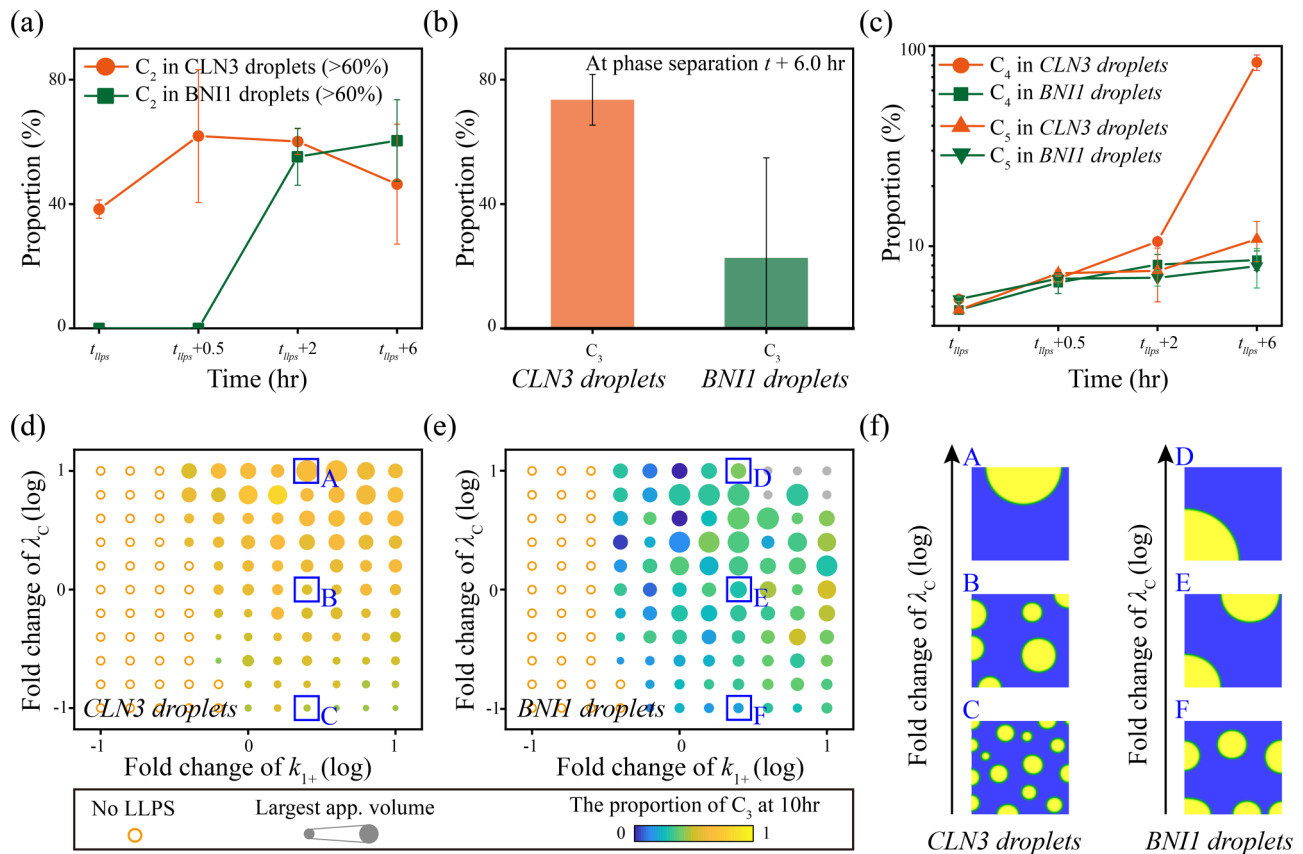
FIG. 4. Differences of higher-order complexes and droplet size between $CLN3$ droplet and $BNI1$ droplet. (a)–(c) Size proportion of higher-order complexes in $CLN3$ droplet and $BNI1$ droplet. (d), (e) Effect of the binding rate (k_{1+}) and the diffusion rate (λ_C) on the patterns of $CLN3$ droplet and $BNI1$ droplet. (f) Three represented cases of droplets evolution in (d) and (e).

and 4(e). Variation of the binding rate (k_{1+}) barely influences the proportion of higher-order complexes in $CLN3$ droplets, but $CLN3$ droplet size is significantly increased with the diffusion rate (λ_C) increases [Fig. 4(d)]. For $BNI1$ droplets, variation of the binding rate (k_{1+}) and the diffusion rate (λ_C) can efficiently adjust the proportion of higher-order complexes and droplet size [Fig. 4(e)]. The proportion of the majority of droplets is gradually increased with the binding rate (k_{1+}) increases, while the droplet size trends to get large with the diffusion rate (λ_C) increases. Three representative cases that exhibit the droplet size increases with the diffusion rate (λ_C) increases of $CLN3$ droplet and $BNI1$ droplet are, respectively, shown in Fig. 4(f).

Obviously, an increase in the diffusion rate results in larger droplet size due to the enhanced fusion of smaller droplets. The distinct responses of the higher-order complex assembly to the binding rate are primarily dominated by the interdroplet pattern of these two types of droplets. C_3 complex rapidly assembles in CLN3 droplets within 0.5 h after phase separation, filling almost the entire droplet [Fig. 3(c)], while C_3 complex only forms a ring structure in BNI1 droplets within 2.0 h, and fills the entire droplet nearly 6.0 h after phase separation [Fig. 3(d)]. Therefore, the fast assembly of

C_3 in CLN3 droplets results in the weak response of higher-order complexes to an increase in the binding rate, while the compared slower assembly of C_3 in BNI1 droplets leads to an enhancement in the proportion of higher-order complexes with an increase in the binding rate.

C. Competitive assembly between different mRNA-driven droplets

$CLN3$ droplets locate around nuclei but $BNI1$ droplets prefers to assemble at cell tips [15]. Previous experimental analysis proposed the lack of colocalization is due to the intrinsic, compositional differences between these two types of droplets [15]. Having dissected the distinct physical properties (Fig. 2) and constituent differences (Figs. 3 and 4) of these two droplets, we sought to explore how $CLN3$ mRNA and $BNI1$ mRNA cooperate or compete with each other, segregating to distinct droplets by sharing Whi3 protein in a common cytoplasm. Hence, a modified phase-field model considering the mix of free $CLN3$ mRNA, $BNI1$ mRNA, and Whi3 protein is developed. $CLN3$ and $BNI1$ severally bind with Whi3 to drive Whi3 LLPS [Fig. 5(a)]. The governing equations for the cooperative control of Whi3 LLPS evolution by $CLN3$ and
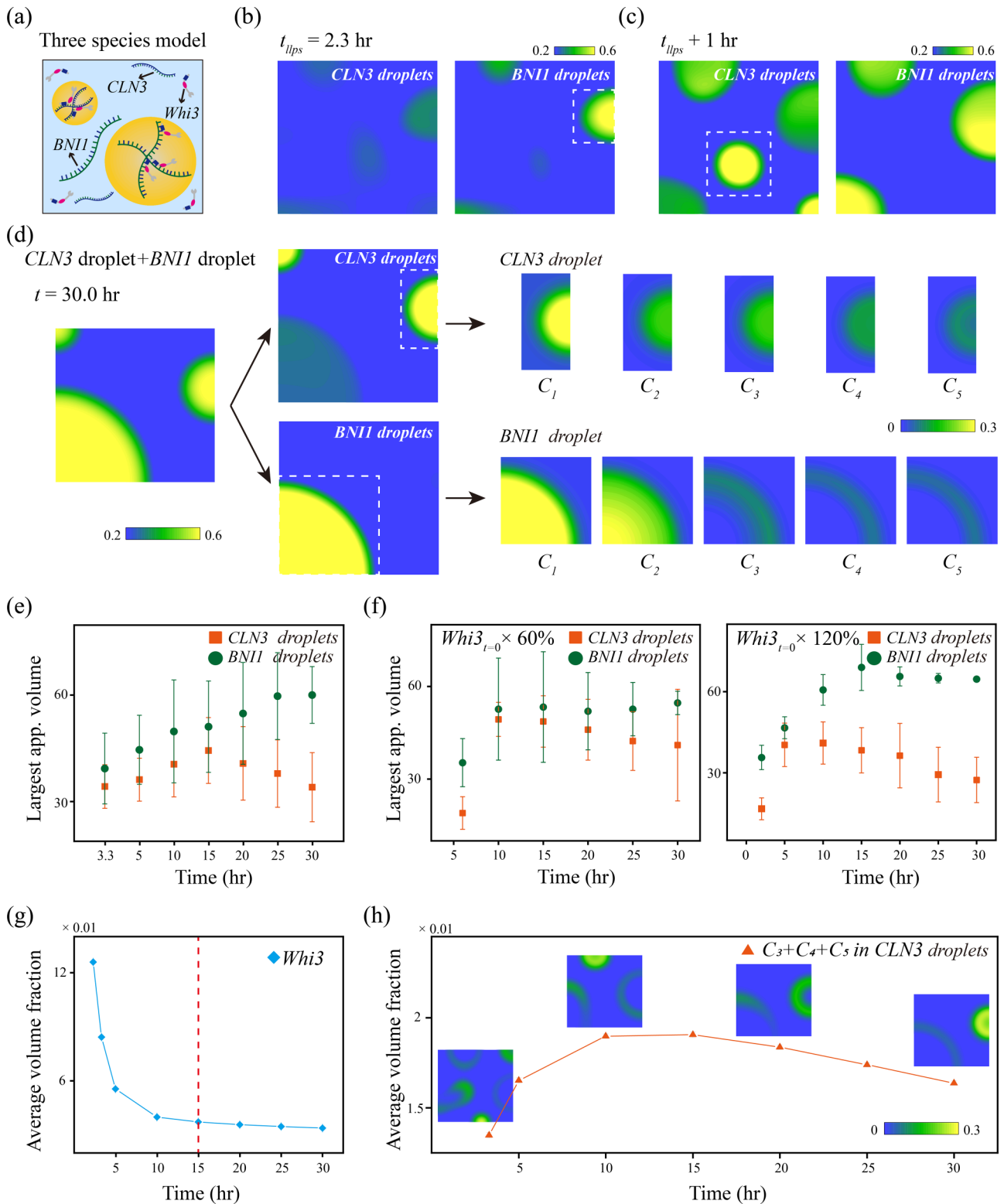
FIG. 5. *CLN*3 and *BNI*1 competitively bind Whi3 to drive phase separation. (a) Schematic diagram of the *CLN*3 mRNA, *BNI*1 mRNA, and Whi3 protein mixed system. (b) Distribution of *BNI*1 and *CLN*3 droplets in phase space when LLPS occurs. (c) Distribution of *BNI*1 and *CLN*3 droplets at 1 h after LLPS occurs. (d) Intradroplet composition analysis of the mixed system at 30 h. (e) Evolution of the largest *CLN*3 and *BNI*1 droplets size in ten independent simulation experiments. (f) Temporal dynamics of free Whi3 level. (g) Evolution of the largest *CLN*3 and *BNI*1 droplets size at two typical initial levels of free Whi3. (h) Evolution of the higher-order complexes in *CLN*3 droplet.

*BNI*1 are presented as follows:

$$\frac{\partial P}{\partial t} = \nabla[\lambda_P M(\phi)\nabla P] + \sum_{i=1}^{5} k_{i-}^{CLN3} C_i^{CLN3} + \sum_{i=1}^{5} k_{i-}^{BNI1} C_i^{BNI1} k_{1-} C_1$$

$$- P\left(k_{1+}^{CLN3} R^{CLN3} + k_{1+}^{BNI1} R^{BNI1} + \sum_{i=2}^{5} k_{i+}^{CLN3} C_{i-1}^{CLN3} + \sum_{i=2}^{5} k_{i+}^{BNI1} C_{i-1}^{BNI1} \right), \tag{16}$$

$$\frac{\partial R^{CLN3}}{\partial t} = \nabla[\lambda_{R^{CLN3}} M(\phi)\nabla R^{CLN3}] + k_{1-}^{CLN3} C_1^{CLN3} - k_{1+}^{CLN3} PR^{CLN3}, \tag{17}$$

$$\frac{\partial R^{BNI1}}{\partial t} = \nabla[\lambda_{R^{BNI1}} M(\phi)\nabla R^{BNI1}] + k_{1-}^{BNI1} C_1^{BNI1} - k_{1+}^{BNI1} PR^{BNI1}, \tag{18}$$

$$\frac{\partial C_i^{CLN3}}{\partial t} = \begin{cases} \nabla\left[\lambda_{C_i^{CLN3}} M(\phi)\nabla\left(\frac{\delta F}{\delta C_i^{CLN3}}\right)\right] + P\left(k_{i+}^{CLN3} R^{CLN3} - k_{i+}^{CLN3} C_i^{CLN3}\right) - k_{i+}^{CLN3} C_i^{CLN3} + k_{(i+1)-}^{CLN3} C_{i+1}^{CLN3}, i = 1 \\ \nabla\left[\lambda_{C_i^{CLN3}} M(\phi)\nabla\left(\frac{\delta F}{\delta C^{CLN3}}\right)\right] + P\left(k_{i+}^{CLN3} C_{i-1}^{CLN3} - k_{(i+1)+}^{CLN3} C_i^{CLN3}\right) - k_{i-}^{CLN3} C_i^{CLN3} + k_{(i+1)-}^{CLN3} C_{i+1}^{CLN3}, i = \{2,3,4\}, \\ \nabla\left[\lambda_{C_i^{CLN3}} M(\phi)\nabla\left(\frac{\delta F}{\delta C_i^{CLN3}}\right)\right] + Pk_{i+}^{CLN3} C_{i-1}^{CLN3} - k_{i-}^{CLN3} C_i^{CLN3}, i = 5 \end{cases} \tag{19}$$

$$\phi = \sum_{i=1}^{5} C_i^{CLN3} + \sum_{i=1}^{5} C_i^{BNI1}, \tag{20}$$

$$F = \int_\Omega \left(\frac{\varepsilon^2}{2}|\nabla\phi|^2 + \frac{\phi^2}{4\omega} \times [1-\phi]^2 \right) dx. \tag{21}$$

Experimental observations have shown that the two types of CLN3 and BNI1 complexes can coexist within the same droplets [15]. Previous theoretical study defined the gradient term of the free energy as the sum of two complexes, which can coexist within the same droplets [20]. Taking into account these studies, the gradient term was thus set as the square of the gradient of the entire sum of CLN3 and BNI1 in our model. Compared to the separate models of *BNI*1 droplet and *CLN*3 droplet (Table I), only the parameters of gradient energy coefficient (ε) and interfacial energy coefficient (ω) in the free-energy term are revised as $\varepsilon = 0.0245$ and $\omega = 0.8$ in the three-species (free *CLN*3 mRNA, *BNI*1 mRNA, and Whi3 protein) mixed model.

In the mixed system, LLPS occurs at about 2.3 h and *BNI*1 droplets are the major component [Fig. 5(b)], suggesting *BNI*1 droplets assemble earlier than *CLN*3 droplets. Then, *CLN*3 could rapidly bind with Whi3 to assemble into new droplets at a different location without incorporating into *BNI*1 droplets at 1 h after LLPS [Fig. 5(c), white dotted box]. These simulation results are consistent with the experimental result that when *CLN*3 was added to Whi3 droplets induced by *BNI*1, *CLN*3 preferentially assembled into new droplets, rather than incorporating into *BNI*1 droplets [15]. The droplets of the mixed system evolve into larger droplets over time, and the size of the droplets remains stable at around 30 h [Fig. 5(d)]. The stable state indicates that CLN3-Whi3 complex and BNI-Whi3 complex are independent of each other and occupy different regions to severally form droplets. *CLN*3 droplet and *BNI*1 droplet retain their distinct physical properties in the mixed system. Similar to previous results (Fig. 3), the size of *BNI*1 droplet is still significantly larger than *CLN*3 [Fig. 5(d)]. As the composition of the stable droplets shown [right panel of Fig. 5(d)], higher-order complexes are approximately uniformly distributed throughout

*CLN*3 droplet, but only form a ring structure at the interface of *BNI*1 droplet.

To dissect the relation between *CLN*3 droplet and *BNI*1 droplet in the mixed system, spatiotemporal evolution of the largest size of these two types of droplets is discussed [Fig. 5(e)]. During the period from the onset of LLPS to 15 h, both the size of *CLN*3 droplet and *BNI*1 droplet gradually increases. The free Whi3 protein in the mixed system rapidly decreases at the onset of LLPS until the 15th hour [Fig. 5(f)], providing the main supply source for the growth of *CLN*3 droplet and *BNI*1 droplet. After 15 h, free Whi3 protein falls to a relatively low level, which is insufficient to sustain droplets growth. Nevertheless, the size of *BNI*1 droplet still increases but the size of *CLN*3 droplet gradually declines after 15 h, implying a potential competition between these two types of droplets [Fig. 5(e)]. *BNI*1 exhibits a significant advantage in competitive binding to Whi3, and the Whi3 that has been recruited in *CLN*3 droplet subsequently becomes the source for the growth of *BNI*1 droplet.

We further examined the competition between *CLN*3 droplet and *BNI*1 droplet at two typical initial levels of free Whi3 [Fig. 5(g)]. Compared to the default system [Fig. 5(e)], both a low (60%) or a high (120%) initial level of Whi3 results in that *BNI*1 droplet size reaches the stable state earlier. The stable *BNI*1 droplet size of high initial Whi3 is bigger than the size of low initial Whi3. Unexpectedly, although the evolution of *BNI*1 droplet size becomes stable, *CLN*3 droplet size still declines over time [Fig. 5(g)], hinting the size decline of *CLN*3 droplet is not completely determined by the competition with *BNI*1 droplet. Though observing the evolution of the higher-order complexes pattern in *CLN*3 droplets [Fig. 5(h)], we found higher-order complexes form ring structure at the droplet interface with large droplet size with sufficient free Whi3 during the early stage. However, the droplet size

gradually decreases since the higher-order complexes appear to spread to the center and uniformly distribute throughout the droplet at the later state with the shortage of free Whi3.

D. Segregation or colocalization droplet patterns captured by demixing energy, mRNA level, and mRNA-protein binding rate

Previous study reported that the distinct properties and the lack of colocalization between *CLN*3 droplet and *BNI*1 droplet are primarily determined by the secondary structure of mRNAs [15]. After disrupting the mRNAs secondary structure by heating, *CLN*3 droplet can readily be incorporated into *BNI*1 droplet. To explore how the segregation or colocalization patterns between *CLN*3 droplet and *BNI*1 droplet are controlled in the mixed system, the transition of droplet patterns is investigated by adjusting the demixing energy. Demixing energy determines whether different species could colocalize within a single droplet. As the results show in Fig. 6(a), for the control mixed system, *CLN*3 and *BNI*1 segregate to different droplets without colocalization (point A, pattern 1). While increasing the gradient energy coefficient (ε), *CLN*3 droplet incorporates into *BNI*1 droplet readily, and the droplet pattern appears as the structure of *BNI*1-core and *CLN*3-shell (point B, pattern 2), which has been experimentally observed using melted *CLN*3 mRNA [15]. For point B, a further increase of the interfacial energy coefficient (ω) induces the *BNI*1 and *CLN*3 complexes to aggregate at a shared interface and to occupy the two poles of the droplet (point 3, pattern 3), which was also identified in experiments with refolded *CLN*3 mRNA [15]. More importantly, synergistically reducing the two energy coefficients (ε and ω) drives a droplet pattern of *CLN*3-core and *BNI*1-shell (point 4, pattern 4), which has not been experimentally identified.

The gradient energy coefficient reflects the spatial nonuniformity of the system, and determines the sensitivity of the free energy to the gradient of the order parameter, while the interface energy coefficient describes the energy difference between different phases. To gain a better understanding of the potential mechanism underlying the formation of the fourth pattern, the effects of the two energy coefficients on Whi3 droplets that were independently driven by CLN3 or BNI1 were compared (Figs. S2 and S3 [35]). With the same initial levels of protein and mRNAs, when the two energy coefficients are small, CLN3 can induce phase separation of Whi3 (Fig. S2 [35]), while BNI1 cannot (Fig. S3 [35]), while in the three-species mixture system, Whi3 concentration tends to be slightly higher around the edge of the CLN3-Whi3 droplets, and BNI1 can snatch the Whi3 in CLN3 droplets [Figs. 5(e)–5(h)]. Therefore, CLN3-Whi3 droplets could provide a favorable microenvironment for BNI1-Whi3 complex assembly around the surface of CLN3-Whi droplets, facilitating the formation of CLN3 core-BLNI1 shell pattern when the two energy coefficients are small.

To assess how different initial levels of mRNAs in the mixed system are able to establish a heterogeneous droplet field, we also varied the initial levels of *CLN*3 and *BNI*1 synergistically [Fig. 6(b)]. As a result, the parametric space is divided into four regions when the droplets sizes are stable at 30 h, including one region without LLPS (region 1) and three regions with specific droplet patterns (regions 2, 3, and 4). In region 1, low initial levels of *CLN*3 mRNA and *BNI*1 mRNA cannot drive phase separation, while an exclusive high level of *BNI*1 or *CLN*3 primarily triggers *BNI*1 droplet (region 2) or *CLN*3 droplet (region 3). Simultaneous relative high levels of *BNI*1 and *CLN*3 in region 4 induce diverse droplet patterns. As the three typical patterns selected from region 4 show [Fig. 6(c)], the droplets exhibit *BNI*1-core and *CLN*3-shell pattern when the level of *CLN*3 is higher than *BNI*1 (point A), while a higher level of *BNI*1 drives the formation of cointerface droplet pattern, and *BNI*1 and *CLN*3 complexes occupy the two poles of the droplet (point B). Relative low levels of *BNI*1 and *CLN*3 segregate these two mRNAs to different droplets without colocalization (point C), controlling the construction of a heterogeneous droplet field.

Besides the initial mRNA levels, the binding of mRNA with protein to form complexes is one of the most important processes that underlies the generation of condensates. Thus, how the strength of the binding rates of the two mRNAs (*CLN*3 and *BNI*1) with Whi3 determine the constituents and spatiotemporal dynamics of droplets are explored as well. The binding rates of the two mRNAs with Whi3 are tuned exponentially and the corresponding droplet patterns at the early (5 h), middle (15 h), and late (30 h) stages are presented [Fig. 6(d)]. Similar to the results of mRNAs initial levels variation [Fig. 6(b)], the parametric space can also be divided into four regions [Fig. 6(d)]. The droplet pattern evolutions of three typical binding rates (points A, B, and C) are presented in Fig. 6(e). Low binding rates [Fig. 6(e), point A] result in the early stage inability to assemble enough complexes to form droplet. As time progresses, the level of complexes reach the threshold for LLPS induction, and the area of region 1 declines [Fig. 6(d)]. Spatiotemporal dynamics of the point A system transform into a mixed phase with the pattern of *BNI*1-core and *CLN*3-shell [Fig. 6(e), point A]. The area of region 2 is increased with time. The system of point B in the mixed-region 4 is close to the *BNI*1 phase region 2, and the entire droplet is strongly dominated by *BNI*1 complex over time [Fig. 6(e), point B]. In contrast, the area of region 3 appears to decline with time. *CLN*3 complex-dominated droplets are less stable, and region 3 contracts towards the bottom right. The system of point C belongs to region 3 with the pattern of *CLN*3 droplet at the initial stage, but subsequently transforms into a mixed phase containing *BNI*1-core and *CLN*3-shell pattern at the late stage [Fig. 6(e), point C].

IV. DISCUSSION

It is now well established that phase separation is an efficient mechanism for cells to achieve biological function [36]. Aberrant forms of condensates are associated with many diseases [2], while much less is understood about the control mechanisms of droplet assembly. Previous studies dissected the distinct physical properties of protein droplets driven by different mRNAs [1,14,15]. *BNI*1 droplet was experimentally determined to fuse faster than *CLN*3 droplet, and the optimal mRNA to Whi3 molar ratio for *BNI*1 is larger than that for *CLN*3 [14]. Our model well reproduces the distinct physical properties of these two types of droplets, and we further found their intradroplet patterns are quite different. The size of *BNI*1 droplet grows faster while the higher-order complexes
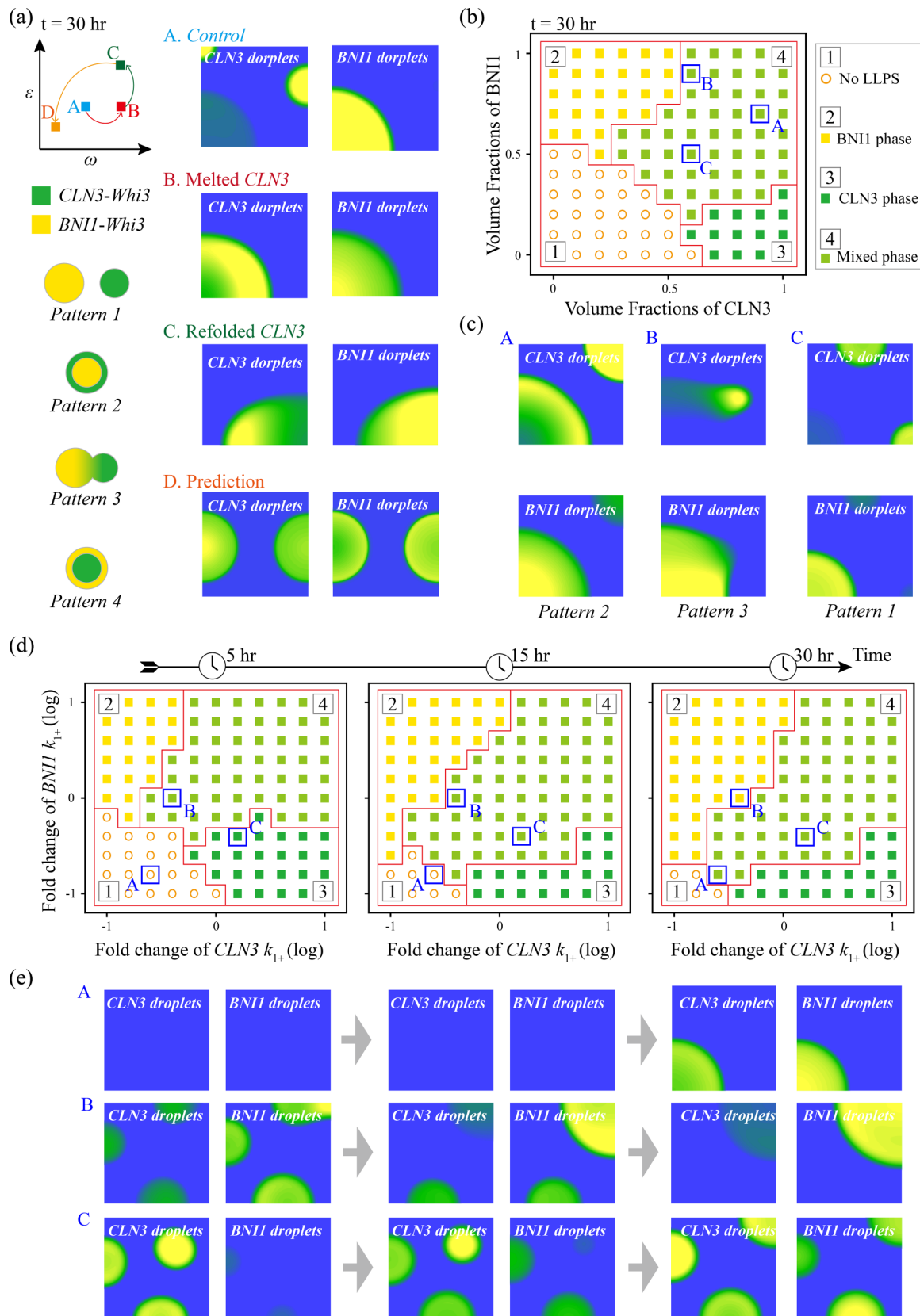
FIG. 6. Regulatory strategies for droplet patterns evolution in the *CLN*3, *BNI*1, and Whi3 mixed system. (a) Role of the demixing energy coefficients in controlling the diverse droplet patterns. (b) Initial levels of mRNAs control the droplet patterns. Four typical phases are no LLPS, *BNI*1 droplet, *CLN*3 droplet, and the pattern of mixed droplets. (c) Three typical droplet patterns in the mixed phase correspond to points A–C indicated in (b). (d) State diagrams of droplet patterns evolution at three timescales vs the binding rates of *CLN*3 and *BNI*1 with Whi3. (e) Three typical droplet patterns evolution correspond to points A–C indicated in (d).

assemble quicker in *CLN*3 droplet. Although both *BNI*1 and *CLN*3 have five Whi3 binding sites, the different features, such as that *CLN*3 is about four times shorter than *BNI*1, might drive the difference in droplet formation and property. Here, we found that the growth rate of droplet size and the higher-order complexes assembly are, respectively, determined by the diffusion rate of droplet and the binding rate of mRNA with protein. Specifically, the physical properties of BNI1 droplet fuse faster than CLN3 droplet obtained in previous experiments that was predicted to be determined by the diffusion rate by our model (Figs. 3 and 4), whereas our model also predicted the properties of higher-order complexes in CLN3 droplet assemble quicker than that in BNI1 droplet, which was further found to be dominated by the binding rate of mRNA with protein. Hence, our analysis suggests that the diffusion rate and mRNA-protein binding rate might be the general and intrinsic mechanisms for determining the physical properties of fusion and higher-order assembly in droplets.

Previous experimental study identified that CLN3 droplets locate around nuclei to regulate cell cycle, while BNI1 droplets locate at cell tips to establish polarity sites and modulate actin. The lack of colocalization and distinct functions of these two droplets were proposed to be determined by their distinct physical properties [15]. Consistent with these findings, our three-species mixed-phase separation model also revealed that BNI1 droplets and CLN3 droplets tend to assemble separately rather than colocalize. Through developing a three-species mixed-phase separation model, we found *BNI*1 droplet and *CLN*3 droplet preferentially assemble separately, rather than by colocalization, which has been experimentally observed [15]. More importantly, a competitive relationship between *BNI*1 and *CLN*3 for binding with Whi3 is identified. *BNI*1 exhibits a significant advantage in the competition through snatching the Whi3 that has been recruited in *CLN*3 droplets when the free Whi3 is lacking. Previous experimental study found that in cells with low expression of Whi3, CLN3 is distributed more uniformly instead of forming clustered droplets within the cell body. On the other hand, BNI1 fails to effectively localize and accumulate in the absence of Whi3, leading to defects in cell polarity establishment [15]. Based on our results from the competition between CLN3 droplets and BNI1 droplets [Figs. 5(e)–5(g)], we speculate that in cells with a certain low-level range of Whi3, executing polarity sites establishment and actin modulation controlled by BNI1 might be the priority choice compared to the functions of cell cycle mediated by CLN3.

Recent study reported that the structure of mRNAs determines the segregation or colocalization of different droplets [15]. Specifically, through heating to disrupt the second structure, *CLN*3 can readily incorporate into *BNI*1 droplets. In our simulation, the colocalization of these two types of droplets can also be obtained by increasing the demixing energy coefficients. Increasing the gradient energy coefficient (ε) drives the droplet pattern to appear as the structure of *BNI*1-core and *CLN*3-shell. Further increasing the interfacial energy coefficient (ω) induces the *BNI*1 and *CLN*3 complexes to aggregate at a shared interface and occupy the two poles of the droplet. Both of these two patterns were experimentally observed in the melted *CLN*3 mRNA- and refolded *CLN*3 mRNA-driven droplet assembly [15]. More importantly, we predicted that

synergistically reducing these two energy coefficients (ε and ω) may drive a new pattern of *CLN*3-core and *BNI*1-shell. In addition, we have shown how the initial mRNAs levels and the complex binding rates maintain the droplet patterns evolution. Besides the predicted droplet pattern of *CLN*3-core and *BNI*1-shell, all the experimental observed patterns can be well achieved by varying the initial mRNAs level or the mRNA-protein binding rate.

Intradroplet pattern determines the properties and functions of droplet condensates, and the coexistence and transition between multiple droplet patterns have important biological implications to perform specific functions [37]. Differences in the surface tensions of droplets constituting the core-shell pattern have been experimentally confirmed [38], The core-shell pattern plays an important role in the process of droplet pattern transition. The complexes that compose the shell of a droplet cannot only capture free molecules in the matrix, but also exchange proteins with the complexes that fill the core of the droplet. These are codetermined by the availability of binding sites and binding rate on the shell and core complexes; furthermore, the shell complexes act as a barrier, restricting the exchange of the core complex with the external matrix, playing a positive role in maintaining the droplet core stably performing specific biological functions.

We identified four typical intradroplet patternings in mixed systems that two mRNAs compete for binding to the same protein partner. When the droplets undergo Oswald ripening and evolve to a near-steady state [20,39,40], the spatiotemporal distributions of different complexes in phase space suggest that a shared interface is established between droplets formed by distinct complexes. Intermolecular multivalent interactions have been pointed to underlie the generation of coexisting liquid phases [38], but the dynamic mechanisms remain unclear. Phase-separated droplets have no physical barriers such as lipid membranes, and their internal components can diffuse freely and dynamically exchange with the surrounding microenvironment [10]. Two droplets sharing an interface may mutually inhibit their contact with the surrounding matrix, but also promote molecular exchange within the droplets. How this inhibitory and promotional behavior leads to a larger macroscopic transformation is currently unclear. Overall, this work provides several insights into the understanding that mRNAs "encode" the physical properties of phase-separated condensates by controlling the spatiotemporal distributions of higher-order complexes, providing potential strategies for further experimental validation and related disease treatment.

Previous studies have suggested that the diffusion coefficients of intracellular molecules depend on their size and cellular context [41]. However, in comparison to experimental data, the effective collective diffusion coefficients of molecules in our model (Table I) are significantly smaller. Multiple factors contributed to the orders of magnitude difference. The size and distribution of droplets have a profound impact on molecules diffusion process. Large droplets occupy more space, impeding the diffusion of surrounding molecules. A nonuniform droplet distribution can lead to molecular concentration gradients in regions where droplet aggregation occurs, further restricting molecules diffusion around the droplets [1,14]. Besides, molecular diffusion is sensitive to intermolecular interactions. Intermolecular interactions can act

as a strong attraction for limiting molecules diffusion. Studies have reported that the RNA-binding protein FUS undergoes a structural compaction upon binding to RNA, resulting in a decreased diffusion coefficient of FUS [42]. The van der Waals attraction is vital to dominate the decrease of molecules diffusion as well [43]. Despite that the droplets emerging *in vitro* are not very dense, the apparent viscosity inside the droplets is very large. Recent study found that the cytoplasm behaves like a liquid for small length scales and a physical gel for larger length scales [44]. A theoretical framework for describing the diffusion of probes and viscosity in complex fluids was also proposed, providing a database for rotational diffusion coefficients and the diffusion coefficients of the sliding of proteins along major grooves of DNA in *Escherichia coli* [45,46]. The dependence of the viscosity on the length scale at which it is probed is ubiquitous [47]. Actually, the molecules that move inside the droplets are large parts of the droplets made by sticky molecules, greatly confining the diffusion of molecules in the RNA-driven Whi3 droplets system. Therefore, the average molecular diffusion coefficient calculated in our model is expected to be lower than that of the free molecules. To fully address how the molecules diffusion proceeds in such a system, a more specific or comprehensive model should be further proposed with the combination of future experimental observations.

A recent study has demonstrated that membrane attachment is a key mechanism for controlling the formation and sizing of condensates throughout the cell [1]. Membranes recruitment of Whi3 directly enhances protein local concentration and favors Whi3 condensation. However, this recruitment also restricts molecular diffusion, limiting the size of Whi3 coarsening. To comprehensively understand the mechanisms underlying the membranes-induced trade-off between enhancing droplet formation and limiting droplets size, further model-based theoretical analysis is urgently required as well. Consistent with these experimental observations, our study also qualitatively determines that both the formation and size of Whi3 droplets are enhanced with increasing concentrations of molecules [Fig. 2(d)] and diffusion rates [Fig. 4(f)]. The sizes of CLN3-Whi3 droplets are significantly smaller than BNI1-Whi3 droplets, which is predicted to be induced by the smaller diffusion rate of CLN3 complexes (Table I). Although our model can qualitatively reproduce the experimental observations of the distinct physical properties of different droplets, and the thorough analysis performed, the

direct evidence to support the ranges of our fit parameters is still lacking. We hope these ranges and our predictions of this study can be tested by experiment in the future.

Although our model could characterize previous experimental observations [14,15] and further explore the patterns formation by various mRNAs, our phase-field model still has several limitations for analyzing the regulation of Whi3 condensates by membranes [1]. First, the complex environment makes it difficult to explicitly model the impact of membranes on molecules diffusion, which we have simplified in our current model by using the parameters of effective diffusion rate (Table I). Considering the diffusion rate of molecules as a function that depends on the local molecular concentration in future efforts will improve our model. Second, the volume fraction of each component containing the required solvent is the basic assumption of our phase-field model, which ignores the possible interactions of mRNA and Whi3 with solvent molecules. *In vitro* experiments suggest that in the presence of low solvent concentration and high Whi3 concentration, small condensates formed by Whi3 can be observed [14]. However, the self-induced assembly of Whi3 cannot be obtained by our model, which may be vital for the formation of small condensates induced by the direct recruitment of Whi3 to membranes.

We estimated our model parameters primarily by replicating three previous experimental observations: (1) BNI1 effectively induces phase separation of Whi3 at low initial concentrations (Fig. 5(b) in Ref. [14]); (2) BNI1 droplets fuse faster than CLN3 droplets (Fig. 5(d) in Ref. [14]); and (3) the optimal RNA to Whi3 molar ratio for BNI1 is twofold larger than that estimated for CLN3 (Fig. 5(c) in Ref. [14]). Three distinct droplet patterns predicted by our model were previously reported in Fig. 3(a) of Ref. [15]. Zipped mathematical code files of the model to generate the results in this study are available from the corresponding authors upon reasonable request.

---

[1] W. T. Snead, T. M. Gerbich, I. Seim, Z. X. Hu, A. S. Gladfelter, and A. P. Jalihal, Membrane surfaces regulate assembly of ribonucleoprotein condensates, Nat. Cell Biol. **24**, 461 (2022).

[2] B. Wang, L. Zhang, T. Dai, Z. R. Qin, H. S. Lu, L. Zhang, and F. F. Zhou, Liquid-liquid phase separation in human health and diseases, Signal Transduct. Target. Ther. **6**, 290 (2021).

[3] S. Mehta and J. Zhang, Liquid-liquid phase separation drives cellular function and dysfunction in cancer, Nat. Rev. Cancer **22**, 239 (2022).

[4] X. Jin, J. E. Lee, C. Schaefer, X. W. Luo, A. J. M. Wollman, A. L. Payne-Dwyer, T. Tian, X. W. Zhang, X. Chen, Y. X. Li, T. C. B. McLeish, M. C. Leake, and F. Bai,

Membraneless organelles formed by liquid-liquid phase separation increase bacterial fitness, Sci. Adv. **7**, eabh2929 (2021).

[5] S. Elbaum-Garfinkle, Y. Kim, K. Szczepaniak, C. C. H. Chen, C. R. Eckmann, S. Myong, and C. P. Brangwynne, The disordered P granule protein LAF-1 drives phase separation into droplets with tunable viscosity and dynamics, Proc. Natl. Acad. Sci. USA **112**, 7189 (2015).

[6] Y. G. Zhao and H. Zhang, Phase separation in membrane biology: The interplay between membrane-bound organelles and membraneless condensates, Dev. Cell **55**, 30 (2020).

[7] S. Boeynaems, S. Alberti, N. L. Fawzi, T. Mittag, M. Polymenidou, F. Rousseau, J. Schymkowitz, J. Shorter, B.

Wolozin, L. Van den Bosch, P. Tompa, and M. Fuxreiter, Protein phase separation: A new phase in cell biology, Trends Cell Biol. **28**, 420 (2018).

[8] H. C. Zhang, S. P. Shao, Y. Zeng, X. T. Wang, Y. Z. Qin, Q. N. Ren, S. Q. Xiang, Y. X. Wang, J. Y. Xiao, and Y. J. Sun, Reversible phase separation of HSF1 is required for an acute transcriptional response during heat shock, Nat. Cell Biol. **24**, 340 (2022).

[9] J. G. Gu, Z. Y. Liu, S. N. Zhang, Y. C. Li, W. C. Xia, C. Wang, H. J. Xiang, Z. J. Liu, L. Tan, Y. Fang, C. Liu, and D. Li, Hsp40 proteins phase separate to chaperone the assembly and maintenance of membraneless organelles, Proc. Natl. Acad. Sci. USA **117**, 31123 (2020).

[10] H. Zhang, X. Ji, P. L. Li, C. Liu, J. Z. Lou, Z. Wang, W. Y. Wen, Y. Xiao, M. J. Zhang, and X. L. Zhu, Liquid-liquid phase separation in biology: Mechanisms, physiological functions and human diseases, Sci. China-Life Sci. **63**, 953 (2020).

[11] Y. X. Wu, L. Ma, S. H. Cai, Z. Zhuang, Z. Y. Zhao, S. H. Jin, W. H. Xie, L. L. Zhou, L. Zhang, J. C. Zhao, and J. Cui, RNA-induced liquid phase separation of SARS-CoV-2 nucleocapsid protein facilitates NF-kappa B hyper-activation and inflammation, Signal Transduct. Target. Ther. **6**, 167 (2021).

[12] B. Y. Shen, Z. M. Chen, C. Y. Yu, T. Y. Chen, M. L. Shi, and T. T. Li, Computational screening of phase-separating proteins, Genom. Proteomics Bioinformatics **19**, 13 (2021).

[13] Z. M. Chen, C. Hou, L. Wang, C. Y. Yu, T. Y. Chen, B. Y. Shen, Y. Y. Hou, P. L. Li, and T. T. Li, Screening membrane-less organelle participants with machine-learning models that integrate multimodal features, Proc. Natl. Acad. Sci. USA **119**, e2115369119 (2022).

[14] H. Y. Zhang, S. Elbaum-Garfinkle, E. M. Langdon, N. Taylor, P. Occhipinti, A. A. Bridges, C. P. Brangwynne, and A. S. Gladfelter, RNA controls PolyQ protein phase transitions, Mol. Cell **60**, 220 (2015).

[15] E. M. Langdon, Y. P. Qiu, A. G. Niaki, G. A. McLaughlin, C. A. Weidmann, T. M. Gerbich, J. A. Smith, J. M. Crutchley, C. M. Termini, K. M. Weeks, S. Myong, and A. S. Gladfelter, mRNA structure determines specificity of a polyQ-driven phase separation, Science **360**, 922 (2018).

[16] C. H. Lee, P. Occhipinti, and A. S. Gladfelter, PolyQ-dependent RNA-protein assemblies control symmetry breaking, J. Cell Biol. **208**, 533 (2015).

[17] C. L. Ren, Y. Shan, P. F. Zhang, H. M. Ding, and Y. Q. Ma, Uncovering the molecular mechanism for dual effect of ATP on phase separation in FUS solution, Sci. Adv. **8**, eabo7885 (2022).

[18] Y. Kubo, S. Tanaka, and Y. Yamazaki, Free-energy model of phase inversion dynamics in binary phase separation, Phys. Rev. E **100**, 022137 (2019).

[19] J. Berry, C. P. Brangwynne, and M. Haataja, Physical principles of intracellular organization via active and passive phase transitions, Rep. Prog. Phys. **80**, 046601 (2018).

[20] K. Gasior, J. Zhao, G. McLaughlin, M. G. Forest, A. S. Gladfelter, and J. Newby, Partial demixing of RNA-protein complexes leads to intradroplet patterning in phase-separated biological condensates, Phys. Rev. E **99**, 012411 (2019).

[21] K. Gasior, M. G. Forest, A. S. Gladfelter, and J. M. Newby, Modeling the mechanisms by which coexisting biomolecular RNA-protein condensates form, Bull. Math. Biol. **82**, 153 (2020).

[22] S. Saha, C. A. Weber, M. Nousch, O. Adame-Arana, C. Hoege, M. Y. Hein, E. Osborne-Nishimura, J. Mahamid, M. Jahnel, L. Jawerth, A. Pozniakovski, C. R. Eckmann, F. Julicher, and A. A. Hyman, Polar positioning of phase-separated liquid compartments in cells regulated by an mRNA competition mechanism, Cell **166**, 1572 (2016).

[23] J. W. Cahn and J. E. Hilliard, Free energy of a nonuniform system. I. Interfacial free energy, J. Chem. Phys. **28**, 258 (1958).

[24] D. Zhou, P. Zhang, and W. E, Modified models of polymer phase separation, Phys. Rev. E **73**, 061801 (2006).

[25] A. Fick, Ueber diffusion, Ann. Phys.-Berlin **170**, 59 (1855).

[26] R. Qin and H. Bhadeshia, Phase field method, Mater. Sci. Technol. **26**, 803 (2010).

[27] C. A. Weber, D. Zwicker, F. Julicher, and C. F. Lee, Physics of active emulsions, Rep. Prog. Phys. **82**, 064601 (2019).

[28] A. B. Li, A. Miroshnik, B. D. Rummel, G. Balakrishnan, S. M. Han, and T. Sinno, A unified theory of free energy functionals and applications to diffusion, Proc. Natl. Acad. Sci. USA **119**, e2203399119 (2022).

[29] J. Shen and X. F. Yang, Numerical approximations of Allen-Cahn and Cahn-Hilliard equations, Discret. Contin. Dyn. Syst. **28**, 1669 (2010).

[30] S. M. Wise, Unconditionally stable finite difference, nonlinear multigrid simulation of the Cahn-Hilliard-Hele-Shaw system of equations, J. Sci. Comput. **44**, 38 (2010).

[31] S. M. Wise, C. Wang, and J. S. Lowengrub, An energy-stable and convergent finite-difference scheme for the phase field crystal equation, SIAM J. Numer. Anal. **47**, 2269 (2009).

[32] F. Xu, Z. Y. Yin, L. G. Zhu, J. Jin, Q. Z. He, X. Li, and J. W. Shuai, Oscillations governed by the incoherent dynamics in necroptotic signaling, Front. Phys. **9**, 726638 (2021).

[33] X. Li, C. Q. Zhong, R. Wu, X. Z. Xu, Z. H. Yang, S. W. Cai, X. R. Wu, X. Chen, Z. Y. Yin, Q. Z. He, D. J. Li, F. Xu, Y. H. Yan, H. Qi, C. C. Xie, J. W. Shuai, and J. H. Han, RIP1-dependent linear and nonlinear recruitments of caspase-8 and RIP3 respectively to necrosome specify distinct cell death outcomes, Protein Cell **12**, 858 (2021).

[34] R. L. Iman, J. C. Helton, and J. E. Campbell, An approach to sensitivity analysis of computer-models.1. Introduction, input variable selection and preliminary variable assessment, J. Qual. Technol. **13**, 174 (1981).

[35] See Supplemental Material at http://link.aps.org/supplemental/10.1103/PhysRevResearch.5.023159 for Fig. S1: Random parameter analysis for testing the reliability of the model's parameter values; Fig. S2: Phase diagrams of CLN3 droplets at four representative time points under different energy coefficients; and Fig. S3: Phase diagrams of BNI1 droplets at four representative time points under different energy coefficients.

[36] J. A. Riback, L. Zhu, M. C. Ferrolino, M. Tolbert, D. M. Mitrea, D. W. Sanders, M. T. Wei, R. W. Kriwacki, and C. P. Brangwynne, Composition-dependent thermodynamics of intracellular phase separation, Nature (London) **581**, 209 (2020).

[37] S. Alberti, A. Gladfelter, and T. Mittag, Considerations and challenges in studying liquid-liquid phase separation and biomolecular condensates, Cell **176**, 419 (2019).

[38] M. Feric, N. Vaidya, T. S. Harmon, D. M. Mitrea, L. Zhu, T. M. Richardson, R. W. Kriwacki, R. V. Pappu, and C. P. Brangwynne, Coexisting liquid phases underlie nucleolar subcompartments, Cell **165**, 1686 (2016).

[39] J. D. Wurtz and C. F. Lee, Chemical-Reaction-Controlled Phase Separated Drops: Formation, Size Selection, and Coarsening, Phys. Rev. Lett. **120**, 078102 (2018).

[40] D. Zwicker, A. A. Hyman, and F. Julicher, Suppression of Ostwald ripening in active emulsions, Phys. Rev. E **92**, 012317 (2015).

[41] R. Milo and R. Phillips, *Cell Biology by the Numbers* (Garland Science, New York, 2015).

[42] L. Emmanouilidis, L. Esteban-Hofer, F. F. Damberger, T. de Vries, C. K. X. Nguyen, L. F. Ibanez, S. Mergenthal, E. Klotzsch, M. Yulikov, G. Jeschke, and F. H.-T. Allain, NMR and EPR reveal a compaction of the RNA-binding protein FUS upon droplet formation, Nat. Chem. Biol. **17**, 608 (2021).

[43] A. M. Kusova, A. E. Sitnitsky, and Y. F. Zuev, Impact of intermolecular attraction and repulsion on molecular diffusion and virial coefficients of spheroidal and rod-shaped proteins, J. Mol. Liq. **323**, 114927 (2021).

[44] K. Kwapiszewska, K. Szczepanski, T. Kalwarczyk, B. Michalska, P. Patalas-Krawczyk, J. Szymanski, T. Andryszewski, M. Iwan, J. Duszynski, and R. Holyst, Nanoscale viscosity of cytoplasm is conserved in human cell lines, J. Phys. Chem. Lett. **11**, 6914 (2020).

[45] K. Makuch, R. Holyst, T. Kalwarczyk, P. Garstecki, and J. F. Brady, Diffusion and flow in complex liquids, Soft Matter **16**, 114 (2020).

[46] T. Kalwarczyk, M. Tabaka, and R. Holyst, Biologistics-diffusion coefficients for complete proteome of Escherichia coli, Bioinformatics **28**, 2971 (2012).

[47] T. Kalwarczyk, N. Ziebacz, A. Bielejewska, E. Zaboklicka, K. Koynov, J. Szymanski, A. Wilk, A. Patkowski, J. Gapinski, H. J. Butt, and R. Holyst, Comparative analysis of viscosity of complex liquids and cytoplasm of mammalian cells at the nanoscale, Nano Lett. **11**, 2157 (2011).